

# A Fundamental Limit in Angle-Voltage Coupling Dynamics: Sensitivity Conservation and Breaking

Xiaoyu Peng, Cong Fu, Zhongze Li, Peng Yang, Zhaojian Wang, Feng Liu, *Senior Member, IEEE*

**Abstract**—This paper presents a novel perspective on understanding how the interaction between phase-angle and voltage dynamics affects the stability of inverter-dominated power systems. To explore this, we analyze Bode's integral of frequency-domain sensitivity functions, which reveals the underlying law that limits the system's ability to reject disturbances. Our finding indicates that, although the “total” sensitivity integrals remain conservative in angle-voltage coupled systems, the coupling reshapes their distribution between phase-angle and voltage dynamics, potentially worsening system stability. This finding is generalized into a fundamental law named *sensitivity conservation* in this paper. In addition to the sensitivity conservation, our work also suggests that the system stability could be improved by appropriately redistributing sensitivity across different frequency bands, diverse devices, or between phase-angle and voltage dynamics. This redistribution, however, must be conducted carefully, as the sensitivity conservation law indicates that improving the performance of one aspect may lead to instability of another. This law cannot be bypassed directly by any controllers with a generic feedback structure, underscoring the fundamental limit of angle-voltage coupling dynamics and fostering a broader understanding of its nature. The proposed mechanism provides a core principle for control design in angle-voltage coupled power systems.

**Index Terms**—power system stability, angle-voltage coupling, inverter-dominated power system, sensitivity function, Bode's integral, waterbed effect.

## I. INTRODUCTION

### A. Motivation and Background

INTEGRATING renewable energy sources with inverter-based interfaces has significantly altered the stability characteristics of power systems [1]. Due to the weak supportive capability of inverters and their overlapped timescale of phase-angle and voltage dynamics, existing studies have recognized a more strengthened angle-voltage coupling in inverter-dominated systems, leading to unprecedented coupled instability for both grid-following (GFL) devices and grid-forming (GFM) devices [2]–[5]. Besides, the desynchronization of phase-angles induced by voltage dip [6] and angle-voltage coupled oscillation [7], [8] are observed more frequently in practice. However, the mechanism of angle-voltage coupling that influences the system dynamics is still unclear. The urgent need for more in-depth investigations of the coupling dynamics primarily motivates this work.

### B. Literature Review

Primary research regarding coupled stability focuses on its time-domain feature, mainly based on state space models. The pioneering works [9], [10] account for the voltage dynamics within the synchronization, but set strict conditions for applicable device models. Then, the angle-voltage interaction is investigated from the perspective of the power flow coupling, thus formulating a compatible framework in [11], [12]. Despite

its advantages for control enhancement, however, the coupling mechanism is not quantified. A passivity-based framework is formulated in [13]. But the construction of storage functions might be tricky and difficult. Then, the damping conservation mechanism proposed in [14] quantifies the coupling's impact by its strength to disperse eigenvalues. According to this theory, the coupling may shift the weakest damping even closer to the imaginary axis, shrinking the stability margin.

In contrast to advances in time-domain studies, frequency-domain-based analysis of angle-voltage coupling has garnered relatively less attention. The latter, however, has valuable interpretations and plays a significant role in the control designs. In power electronics studies, decoupling controls have been extensively studied. Specifically, the active-reactive power decoupling strategies for GFM devices are investigated, showing remarkable performance to suppress the angle-voltage coupling under varied system strengths [2], [15]. The dominant factors of power coupling are quantitatively studied with a uniform GFM model [8], [16]. For GFL devices, the impact of terminal voltage dynamics on the synchronization of phase-angles is investigated in [17]. Furthermore, the virtual impedance method also shows its effectiveness in suppressing the angle-voltage coupling [18]. Despite their merits, these methods face challenges when handling systems with hybrid GFM-GFL integration [19]. To address this problem, a general admittance model is formulated to analyze and suppress the coupled oscillation in hybrid GFM-GFL systems [20], [21]. It is imperative to acknowledge that these studies primarily emphasize the interaction between active and reactive power, which, while closely related, is fundamentally different from the coupling between angle and voltage.

Pioneering works have guided the control of angle-voltage coupling, yet its dynamics remain underexplored due to the lack of theoretical tools for uniform analysis. Existing literature often requires tailored analyses for specific network topologies or device models. First, it is important to note that many frequency-domain methods are mainly developed for high R/X distribution grids, assuming parallel networks or using infinite bus representations, which complicates application to meshed transmission systems [14]. Second, these methods focus on the power coupling of inverter-interfaced devices. Despite its close relation, angle-voltage coupling is a distinct issue needing detailed study [13]. To the authors' knowledge, frequency-domain analysis of angle-voltage coupling in transmission grids is still preliminary.

### C. Main Contribution

**Key idea.** In this work, we address the challenge mentioned above using Bode's sensitivity integral [22]. This renowned technique establishes fundamental performance limitations of

dynamic systems that cannot be directly surpassed by control designs within typical feedback structures [23]. Surprisingly, it has received little attention in the community of power system dynamics. Here, for the first time, we employ it to explore fundamental difficulties in tackling angle-voltage coupling in the frequency domain. Since this methodology imposes minimal restrictions on system dynamics [24], it can offer generic results that are adaptable to various device dynamics and grid topologies.

**Main Contribution.** We first extend the multi-input, multi-output version of Bode's integral from singular value [24], [25] to eigenvalue spectrum. Applying the developed theory to the analysis of angle-voltage coupling dynamics reveals that the coupling redistributes the sensitivity integral between phase-angle and voltage dynamics and thus influences the system dynamic characteristics, although its summation remains conservative. In addition, the coupling formulated by power flows usually alters the sensitivity distribution to the direction of worsening the stability. Compared to existing works, the proposed mechanism leverages its wide applicability to various network topologies and devices with hybrid synchronization mechanisms (GFM or GFL) and distinct control strategies. Therefore, it provides a uniform and generic approach to analyzing the coupling dynamics of inverter-dominated power systems. Despite the sensitivity conservation, our results suggest that stability could be enhanced by appropriately redistributing sensitivity across different frequencies, devices, or between phase-angle and voltage dynamics.

**Implications.** Our findings shed new light on the control design of inverter-dominated power systems with strong angle-voltage coupling. Specifically, we showcase and validate a parameter tuning method based on the proposed theory through preliminary tests. Moreover, our theoretical result indicates that improving the performance of one aspect may lead to deterioration of others. For example, non-intuitively, enhancing the synchronization capability through phase-angle regulation can result in worse voltage dynamics. This paper offers a theoretical foundation to facilitate the control design in coupled power systems while avoiding unexpected instability.

#### D. Paper Organization

The rest of this paper is organized as follows: Section II introduces the power system models and formulates the problem. The formal demonstration of sensitivity conservation and breaking is provided in Section III. The simulation analysis is performed on several standard IEEE benchmark systems in Section IV. In Section V, we extend the proposed theory from pure GFM-integrated systems to those with hybrid GFM-GFL devices. Finally, Section VI concludes the paper.

## II. PROBLEM FORMULATION

Consider an  $n$ -bus power system  $\mathcal{G} = G(\mathcal{V}, \mathcal{E})$ , where  $\mathcal{V}$  and  $\mathcal{E}$  are the set of buses and transmission lines, respectively. Each bus  $i \in \mathcal{V}$  has port-wise dynamics  $(V_i, \theta_i, P_i, Q_i)$  representing voltage magnitude, phase-angle, active, and reactive power. The vector form  $V = [V_1, V_2, \dots, V_n]^T$  is employed and similar for  $\theta, P$  and  $Q$ . The linearization is conducted around an equilibrium as we focus on small-signal stability analysis.

#### A. Network Dynamic Model

The network coupling is induced by the power flows

$$\begin{aligned} P_i &= V_i \sum_{j \in \mathcal{V}} V_j (G_{ij} \cos \theta_{ij} + B_{ij} \sin \theta_{ij}) \\ Q_i &= V_i \sum_{j \in \mathcal{V}} V_j (G_{ij} \sin \theta_{ij} - B_{ij} \cos \theta_{ij}) \end{aligned} \quad (1)$$

where  $\theta_{ij} = \theta_i - \theta_j$ . By linearizing it around an equilibrium, we can obtain

$$\begin{bmatrix} \Delta P \\ \Delta Q \end{bmatrix} = \begin{bmatrix} \partial P / \partial \theta & \partial P / \partial V \\ \partial Q / \partial \theta & \partial Q / \partial V \end{bmatrix} \begin{bmatrix} \Delta \theta \\ \Delta V \end{bmatrix} \quad (2)$$

where  $\Delta$  denotes the increment w.r.t. the steady value. For brevity, we denote the network coupling matrix as  $H_{\text{net}}$  with following blocks

$$H_{\text{net}} \stackrel{\text{def}}{=} \begin{bmatrix} \partial P / \partial \theta & \partial P / \partial V \\ \partial Q / \partial \theta & \partial Q / \partial V \end{bmatrix} \stackrel{\text{def}}{=} \begin{bmatrix} H_{P\theta} & H_{PV} \\ H_{Q\theta} & H_{QV} \end{bmatrix} \quad (3)$$

The matrix  $H_{\text{net}}$  can be split into two parts  $H_{\text{net}}^{(n)}$  and  $H_{\text{net}}^{(c)}$ , which represent the non-coupled part and angle-voltage coupling, respectively.

$$H_{\text{net}} = \begin{bmatrix} H_{P\theta} & H_{PV} \\ H_{Q\theta} & H_{QV} \end{bmatrix} + \begin{bmatrix} & H_{PV} \\ H_{Q\theta} & \end{bmatrix} \stackrel{\text{def}}{=} H_{\text{net}}^{(n)} + H_{\text{net}}^{(c)} \quad (4)$$

where the quantities with superscripts  $(n)$  and  $(c)$  represent **non-coupled** and **coupled**, respectively.

#### B. Device Dynamic Model

The device dynamics vary depending on their control strategies. Due to the proposed method's generality, we use a unified model as shown below.

$$-\begin{bmatrix} \Delta \theta \\ \Delta V \end{bmatrix} = \begin{bmatrix} G_{\theta P}(s) & G_{\theta V}(s) \\ G_{\theta Q}(s) & G_{VQ}(s) \end{bmatrix} \begin{bmatrix} \Delta P \\ \Delta Q \end{bmatrix} \stackrel{\text{def}}{=} G(s) \begin{bmatrix} \Delta P \\ \Delta Q \end{bmatrix} \quad (5)$$

where  $G_{\theta P}(s)$  and  $G_{VQ}(s)$  are diagonal matrices. For example, the entry-wise expression of  $G_{\theta P}(s)$  is  $\text{diag}(G_{\theta P,1}, G_{\theta P,2}, \dots, G_{\theta P,n})$ , where  $G_{\theta P,i}$  is the phase-angle regulation with its active power injection for the  $i$ -th GFM device. In practical inverter controllers, the cross-loop dynamics are usually not considered, i.e.,  $G_{\theta V}(s) = G_{\theta Q}(s) \approx 0$ . So we focus on  $G_{\theta P}(s)$  and  $G_{VQ}(s)$ . Nevertheless, it should be noted that the proposed methodology is sufficiently robust to account for both network-induced and device cross-loop induced couplings. It is important to highlight that the validity of the core results is independent of the device dynamics decoupled model.

Both  $G_{\theta P}(s)$  and  $G_{VQ}(s)$  have two components: one representing the control strategy  $\tilde{G}_{\theta P,i}$  and  $\tilde{G}_{VQ,i}$  and the other representing the physical lag effect  $G_{\text{lag},i}$ . Some typical control strategies  $\tilde{G}_{\theta P,i}$  and  $\tilde{G}_{VQ,i}$  are listed in Table I, the majority of which are first summarized in [8]. After the control strategies selected, the  $Q - V$  dynamics of the  $i$ -th device can be modeled by  $G_{VQ,i} = \tilde{G}_{VQ,i} G_{\text{lag},i}$ , where  $G_{\text{lag}}$  represent the lag effect induced by the inner loops. A similar procedure can also be conducted for  $P - \theta$  dynamics to derive  $G_{\theta P,i}$ .

This paper focuses on the electromechanical models as it is still the primary concern of transmission system operators. The proposed method can be extended to more practical systems, which are summarized below.

TABLE I  
BRIEF SUMMARY OF INVERTER CONTROL STRATEGIES

| active power control                | $\tilde{G}_{\theta P,i}(s)$          | reactive power control    | $\tilde{G}_{VQ,i}(s)$     |
|-------------------------------------|--------------------------------------|---------------------------|---------------------------|
| $P - \theta$ droop                  | $\frac{1}{k_p}$                      | $Q - V$ droop             | $\frac{1}{k_q}$           |
| $P - \omega$ droop                  | $\frac{1}{k_p s}$                    | $Q - \frac{dV}{dt}$ droop | $\frac{1}{k_q s}$         |
| improved $P - \omega$ droop         | $\frac{1}{k_p s} + \frac{1}{k_{pd}}$ | improved $Q - V$ droop    | $\frac{1}{k_q} + k_{qds}$ |
| virtual synchronous generator (VSG) | $\frac{1}{(Ms+d)s}$                  | voltage inertia           | $\frac{1}{Js+k_q}$        |

- **Consideration of Electromagnetic Dynamics:** Given the generality of the proposed method, it is easy to incorporate electromagnetic models through a standard transformation from a state-space model to a transfer function model if required. In particular, the inner-loop dynamics, such as current and voltage loops of inverters, can be analogously modeled in  $G_{\text{lag},i}$ . Examples can be found in [2] and [26]. In the simulations, we have considered the voltage loop dynamics as an example. More details are provided in Appendix B of [27].<sup>1</sup>

- **Extension to Hybrid GFM-GFL Systems:** The quantities  $[\Delta P^T, \Delta Q^T]^T$  and  $[\Delta\theta^T, \Delta V^T]^T$  are selected as input and output of transfer functions, respectively. Under such selection, only GFM devices can maintain the properness of  $G_{\theta P,i}$  and  $G_{VQ,i}$ . However, another crucial category of devices, GFL inverters, has an inverse input-output relationship, i.e., from  $[\Delta\theta^T, \Delta V^T]^T$  to  $[\Delta P^T, \Delta Q^T]^T$ . Simply taking its inverse might induce non-causality of transfer functions and thus does not match the above theoretical framework. This problem serves as a common difficulty for frequency-domain-based analysis methods of angle-voltage coupling when considering hybrid GFM-GFL integrations. However, the proposed method can apply to hybrid systems by modeling GFL devices in a dynamic network, which will be discussed in Section V.

### C. System Model and Sensitivity Function

Combining the network and device models, the closed-loop system can be formulated in a feedback-interconnected form as shown in Fig. 1(a). Denote by  $L(s) = G(s)H_{\text{net}}$  the open-loop transfer function. Then, the closed-loop system is

$$y = (I + L)^{-1} \cdot \varepsilon + (I + L)^{-1}G \cdot u \stackrel{\text{def}}{=} S \cdot \varepsilon + T \cdot r \quad (6)$$

where the *sensitivity* function  $S(s)$  and its complement  $T(s)$  quantify the disturbance rejection capability w.r.t. disturbances  $\varepsilon$  and the tracking performance w.r.t. reference  $r$ , respectively.

This paper focuses on the sensitivity function  $S$ . For a given frequency  $\omega$ , the smaller its modulus of eigenvalues  $\sigma(S(j\omega)) \stackrel{\text{def}}{=} |\lambda(S(j\omega))|$ , the better the system's ability to suppress disturbance  $\varepsilon$ . Specifically,  $\sigma(S(j\omega)) < 1$ , or equivalently  $\log \sigma(S(j\omega)) < 0$ , is desired, which means the system will not amplify disturbances. Alternatively, the sensitivity can be understood from robustness as the distance between the generalized Nyquist curve of  $\lambda(L(s))$  and  $(-1, 0j)$  satisfies  $\text{dist}(-1, \lambda(L(j\omega))) = |1 + \lambda(L(j\omega))| = \sigma(S(j\omega))^{-1}$ .

<sup>1</sup>Due to space limitations, all appendices are omitted and the full version can be found on the online server [27].

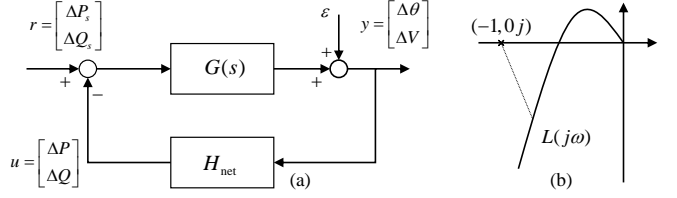


Fig. 1. (a): closed-loop model of power systems. (b): geometrical interpretation of the sensitivity function. The absolute value of the sensitivity indicates the inverse of the distance from the generalized Nyquist curve to  $(-1, 0j)$ .

Similar to  $\mathcal{G}$ , we denote by  $\mathcal{G}_n$  the system with the coupling term  $H_{\text{net}}^{(c)}$  canceled, i.e., treat  $H_{\text{net}}^{(n)}$  as  $H_{\text{net}}$ , with corresponding  $L_n = GH_{\text{net}}^{(n)}$  and  $S_n = (I + L_n)^{-1}$ . Physically, the non-coupled system  $\mathcal{G}_n$  indicates the *ideal* system where the coupling between phase-angle and voltage dynamics is small enough and ignorable.

Next, we show that the sensitivity indicates the internal stability of the feedback system under reasonable conditions, summarized as the following theorem.

**Theorem 1.** Suppose the transfer matrix  $G(s)$  is rational, proper, and does not have right-half-plane poles. Besides, no right-half-plane pole-zero cancellations exist for  $G(s)$  and  $H_{\text{net}}$ . Then,  $S(s)$  is stable if and only if the feedback system is internally stable<sup>2</sup>, i.e., the following transfer-function matrix is stable:

$$\begin{bmatrix} y \\ u \end{bmatrix} = \begin{bmatrix} (I + GH_{\text{net}})^{-1} & (I + GH_{\text{net}})^{-1}G \\ (I + H_{\text{net}}G)^{-1}H_{\text{net}} & (I + H_{\text{net}}G)^{-1}H_{\text{net}}G \end{bmatrix} \begin{bmatrix} \varepsilon \\ r \end{bmatrix} \quad (7)$$

*Proof.* It can be found in Appendix A of [27].  $\square$

The pole condition of  $G(s)$  is easy to satisfy. For properly designed devices, their controllers  $G(s)$  should be open-loop stable (note the potential pure integral  $s$  in denominators of  $\tilde{G}_{\theta P}$  corresponds to the power flow rotation symmetry and thus does not influence the practical stability). Moreover,  $H_{\text{net}}$  is a constant real matrix. Therefore, this theorem suggests that focusing on  $S(s)$  is usually sufficient for the analysis of internal stability, which can be done using well-established theoretical tools such as generalized Nyquist plot, absolute stability, etc. These methods are not the focus of this paper and are thus omitted here.

Before ending this part, we note that the following analysis methods developed based on the sensitivity function are fully model-free and thus applicable to gray-box or even black-box devices. This is because the sensitivity function can be obtained through a standard frequency-scanning technique, which is a common advantage of the frequency-domain methods for the angle-voltage coupling analysis.

### D. Classifying Eigenvalues of Sensitivity Function

There are  $2n$  eigenvalues for the sensitivity function  $S(s)$  of  $\mathcal{G}$ . We denote the index set of all eigenvalues by  $\mathcal{I}$ , which can be classified into the phase-angle induced one  $\mathcal{I}_A$  and the voltage induced one  $\mathcal{I}_V$ . It follows that  $\mathcal{I} = \mathcal{I}_A \cup \mathcal{I}_V = \{1, 2, \dots, 2n\}$  and  $\mathcal{I}_A \cap \mathcal{I}_V = \emptyset$ . It is worth noticing that

<sup>2</sup>The definition of internal stability here is slightly different from the classical one [28]. However, the equivalence of both is easy to verify.

the classification cannot be directly derived from participant factor analysis since the phase-angles' and voltages' participant factors of an eigenvalue might be in the same order in a strongly coupled system. Therefore, this method might fail to distinguish the actual origin of an eigenvalue. On the contrary, this paper adopts a homotopic-map-based method introduced in our previous work. The idea is first proposed in [14] and then developed in [29]. Here, we briefly introduce the idea.

We focus on the network matrix  $H_{\text{net}}$  as the coupling attributed to its off-diagonal part. Define the homotopic map:

$$\mathcal{H}_{\text{net}}(\mu) = (1 - \mu)H_{\text{net}}^{(n)} + \mu H_{\text{net}}^{(c)} \quad (8)$$

It is clear  $\mathcal{H}_{\text{net}}(0) = H_{\text{net}}^{(n)}$  and  $\mathcal{H}_{\text{net}}(1) = H_{\text{net}}$ . Correspondingly, the sensitivity  $\mathcal{S}(\mu) = [I + G\mathcal{H}_{\text{net}}(\mu)]^{-1}$  is defined. The matrix  $H_{\text{net}}^{(n)}$  and the corresponding  $S_n$  are naturally decoupled for phase-angle and voltage dynamics and exhibit a block diagonal structure as shown below. As a result, its eigenvalues are naturally classified into angle-related and voltage-related groups.

$$S_n = (I + L_n)^{-1} = \begin{bmatrix} (I + G_{\theta P} H_{P\theta})^{-1} & \\ & (I + G_{VQ} H_{QV})^{-1} \end{bmatrix} \quad (9)$$

After the eigenvalues of  $\mathcal{S}(0) = S_n$  are classified, the eigenvalues of  $\mathcal{S}(1) = S$  can be classified by tracking their changes when  $\mu$  increases from 0 to 1. Details regarding the eigenvalue tracking method can be found in [29].

### III. SENSITIVITY CONSERVATION AND ITS BREAKING REGARDING ANGLE-VOLTAGE COUPLING DYNAMICS

#### A. Sensitivity Conservation of Angle-Voltage Coupled Systems

This section aims to identify a quantity that remains conservative in the context of angle-voltage coupling dynamics. To this end, we present the following theorem, which establishes a theoretical foundation for achieving this objective.

**Theorem 2.** Consider a system as shown in Fig. 1(a). Suppose that all entries of its open-loop transfer function  $L(s) = G(s)H_{\text{net}}$  are rational, proper. Besides, it has more than one pole-zero excess, and no open-right-half poles. All singular values of  $S(s)$  defined in (6) have constant multiplicity over  $s \in \bar{C}_+$ , where  $\bar{C}_+$  is the closure of the open-right-half plane. If the closed-loop system is stable, then:

$$\sum_{i \in \mathcal{I}} \int_0^\infty \log \sigma_i(S(j\omega)) d\omega = 0 \quad (10)$$

where  $\{\sigma_i(s)\}_{i=1}^{2n}$  denotes the (absolute) eigenvalue spectrum.

*Proof.* The proof can be found in Appendix A of [27].  $\square$

**Applicability of Theorem 2:** The theorem holds universally since the mentioned conditions are commonly satisfied in practice as demonstrated below:

- Noticing the network coupling  $H_{\text{net}}$  is constant, the characterization of the open-loop transfer function mainly relies on the device dynamics  $G(s)$ . Any properly designed device should not have open-right-half poles to ensure internal stability. Otherwise, device- or station-wise instability issues might appear, which is out of our concerns on system-wise stability. Thus, the pole condition generally holds for practical systems.

- The relative degree condition is also easily satisfied, considering the widespread existence of lag effects in inverter-interfaced devices. The inner loop dynamics, including the voltage loop, current loop, and LCL filter dynamics, always generate control lags, which are usually modeled as an inertia transfer function with one relative degree, see [26] and Appendix B of [27] for more details. Moreover, the measurement, communication, computation, and PWM impulse generation also produce pure time delay  $T_d$ , which can be approximated by lags [30], [31]. Combining it with the positive relative degree of control strategies required by the causality, the total relative degree exceeds two and thus meets the requirements.
- As an example, we note that the power systems integrated with any device dynamics as shown in Table I, which cover the most acknowledged inverter dynamics in practical grids. For these systems, after properly modeling their inherent dynamic delays, all of them satisfy the above conditions and thus follow the results of Theorem 2, which suggests the wide compatibility of the proposed method.

It is worth noting that Theorem 2 does not require a specific form of  $L$  and the network  $H_{\text{net}}$  but only relies on some gentle requirements such as relative degree as discussed above. Therefore, it also holds for the non-coupled system  $\mathcal{G}_n$ . In this case, the system's angle and voltage-related subsystems are independent, and we have

$$\underbrace{\sum_{i \in \mathcal{I}_A} \int_0^\infty \log \sigma_i(S_n(j\omega)) d\omega}_{\mathcal{A}_{\mathcal{I}_A}(S_n)} + \underbrace{\sum_{i \in \mathcal{I}_V} \int_0^\infty \log \sigma_i(S_n(j\omega)) d\omega}_{\mathcal{A}_{\mathcal{I}_V}(S_n)} = 0 \quad (11)$$

Due to the anti-diagonal entries of  $H_{\text{net}}$  introduced by  $H_{\text{net}}^{(c)}$ , phase-angle and voltage dynamics are coupled for  $S$ . Then, both integrals are usually non-zero. However, since the conditions of Theorem 2 still hold for the coupled models as soon as we notice the dynamic models solely rely on the devices, the conservation law still holds for the whole coupled system, written as

$$\underbrace{\sum_{i \in \mathcal{I}_A} \int_0^\infty \log \sigma_i(S(j\omega)) d\omega}_{\mathcal{A}_{\mathcal{I}_A}(S)} + \underbrace{\sum_{i \in \mathcal{I}_V} \int_0^\infty \log \sigma_i(S(j\omega)) d\omega}_{\mathcal{A}_{\mathcal{I}_V}(S)} = 0 \quad (12)$$

For brevity, the four terms in (11) and (12) are respectively denoted as  $\mathcal{A}_{\mathcal{I}_A}(S_n)$ ,  $\mathcal{A}_{\mathcal{I}_V}(S_n)$ ,  $\mathcal{A}_{\mathcal{I}_A}(S)$  and  $\mathcal{A}_{\mathcal{I}_V}(S)$ , where  $\mathcal{A}$  denotes the *directed area* following the geometric interpretation of the integral. Then, the sensitivity conservation can be characterized as follows.

**Sensitivity Conservation:** As indicated by (11) and (12), the coupling between phase-angle and voltage dynamics does not change the total amplitude of the sensitivity integral. That is, the sensitivity integral of the overall system remains zero whether the coupling is omitted ( $\mathcal{A}_{\mathcal{I}_A}(S_n) + \mathcal{A}_{\mathcal{I}_V}(S_n) = 0$ ) or considered ( $\mathcal{A}_{\mathcal{I}_A}(S) + \mathcal{A}_{\mathcal{I}_V}(S) = 0$ ).

**Remark 1.** As a corollary of Theorem 2, there exists an alternative formulation of the sensitivity conservation as summarized below: *A system  $\mathcal{G}$  described by Theorem 2 satisfies  $\sum \Re[p(G(s))] = \sum \Re[p(S(s))]$ , where  $\Re(\cdot)$  denotes the real*

part of a complex number and  $p(\cdot)$  represents poles of a transfer function. The proof directly follows from combining Theorem 2 and [32]. As the real part of a pole is usually associated with the damping effect, the corollary indicates the coupling does not change the summation of all dampings, but redistributes it through network feedback. The result provides a frequency-domain explanation of [14].

### B. Breaking of Sensitivity Conservation in Angle-Voltage Coupling Dynamics

Although the sensitivity integral keeps conservation across the overall system, it is redistributed between phase-angle and voltage dynamics through the coupling. As a matter of fact, We find  $\mathcal{A}_{\mathcal{I}_A}(S) = -\mathcal{A}_{\mathcal{I}_V}(S) \neq 0$  always holds in practice.

1) *Single-device non-coupled system*: : We start with the simplest situation, i.e., the single-device system without considering the angle-voltage coupling. In this situation,  $\mathcal{A}_{\mathcal{I}_A}(S_n) = \mathcal{A}_{\mathcal{I}_V}(S_n) = 0$  holds, indicating that suppressing either the phase-angle or voltage disturbances in one frequency band must be compensated by decreasing the robustness in certain other frequencies. This phenomenon is referred to as “waterbed effect” in the control of single-input-single-output systems [23], [25].

2) *Single-device coupled system*: : Based on 1), by introducing the coupling term, the compensation in the single-device system is extended to not only between frequencies but also quantities. For example, if the coupling forces the sensitivity redistributed as  $\mathcal{A}_{\mathcal{I}_A}(S) = -\mathcal{A}_{\mathcal{I}_V}(S) > 0$ , the positive integral value might reduce the disturbance rejection capability of phase-angle dynamics while improving that of voltage dynamics.

3) *Multiple-device coupled system*: : The analysis can be further extended from single-device systems in 1) and 2) to multiple-device systems. In this circumstance, the conservation equation (12) implies that sensitivity redistribution can also occur among devices in addition to frequencies and quantities, which is insightful for coordinated control design.

The above discussions focus on the integral  $\int \log \sigma(S) d\omega$ . It generally serves as a metric for the maximum sensitivity  $\max \log \sigma(S)$  attributed to the concept of available bandwidth [23]. To show this, we present the following theorem.

**Theorem 3.** Suppose the conditions of Theorem 2 and the following bounds are satisfied for any  $i$ -th eigenvalue:

- $\sigma_i(L(j\omega)) \leq e_i/\omega^{k_i+1} \leq c_i < 1/2, \forall \omega \in [\omega_i^c, \infty)$
- $\sigma_i(S(j\omega)) \leq \alpha_i, \forall \omega \in [0, \omega_i^d]$

where,  $\omega_i^c$  is the available bandwidth;  $e_i$ ,  $k_i$ ,  $c_i$ ,  $\alpha_i$  and  $\omega_i^d < \omega_i^c$  are positive constants. Then, the following inequalities hold:

$$\begin{aligned} \max_{\substack{i \in \mathcal{I}_A \\ \omega \in [\omega_i^d, \omega_i^c]}} \log \sigma_i(S(j\omega)) &\geq \frac{\mathcal{A}_{\mathcal{I}_A}(S) + \sum_{i \in \mathcal{I}_A} \left[ \omega_i^d \log \frac{1}{\alpha_i} - \frac{3c_i \omega_i^c}{2k_i} \right]}{n \max_{i \in \mathcal{I}_A} (\omega_i^c - \omega_i^d)} \\ \max_{\substack{i \in \mathcal{I}_V \\ \omega \in [\omega_i^d, \omega_i^c]}} \log \sigma_i(S(j\omega)) &\geq \frac{\mathcal{A}_{\mathcal{I}_V}(S) + \sum_{i \in \mathcal{I}_V} \left[ \omega_i^d \log \frac{1}{\alpha_i} - \frac{3c_i \omega_i^c}{2k_i} \right]}{n \max_{i \in \mathcal{I}_V} (\omega_i^c - \omega_i^d)} \end{aligned} \quad (13)$$

*Proof.* It can be found in Appendix A of [27]. □

**Applicability of Theorem 3:** The constants in the theorem are first explained with an illustration in Fig.2. Due to various factors such as under-modeling, sensor noise, and plant bandwidth, the open-loop gain on the high-frequency band above the available bandwidth  $\omega_i^c$  is desired to decrease for the system’s stability and robustness. Usually, the magnitude of  $\omega_i^c$  is close to the well-known bandwidth of the closed-loop system  $\omega_i^b$ . The constants  $e_i$  and  $k_i$  quantify its decreasing ratio. The second condition is the general design goal, as we usually want the closed-loop system to suppress the disturbances under a given (but also limited) frequency band  $\omega_i^d$  with the rejection capability quantified by  $\alpha_i$ . Therefore, the conditions of Theorem 3 are commonly satisfied.

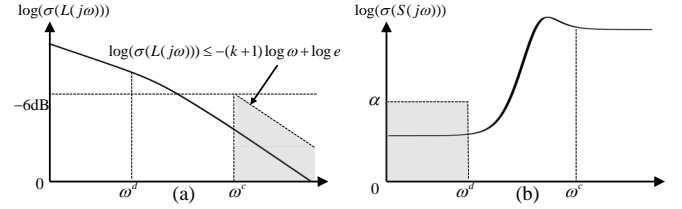


Fig. 2. Illustration of conditions in Theorem 3. (a): the restriction on the open-loop transfer function  $L(s)$ , i.e., the high-frequency gain should decrease. (b): the restriction on the closed-loop sensitivity  $S(s)$ , i.e., the low-frequency gain should be bounded.

Theorem 3 suggests that the breaking of sensitivity conservation may worsen the stability of at least one of the quantities. Still take  $\mathcal{A}_{\mathcal{I}_A} = -\mathcal{A}_{\mathcal{I}_V} > 0$  as an example. Theorem 3 indicates that  $\mathcal{A}_{\mathcal{I}_A} > 0$  increases the lower bound of  $\max \log \sigma_i(S(j\omega))$  for  $i \in \mathcal{I}_A$ . As a result, the weakest mode to reject phase-angle disturbance will be further weakened.

An alternative perspective to understand Theorem 3 is as follows. Noticing the sensitivity conservation  $\mathcal{A}_{\mathcal{I}_A} + \mathcal{A}_{\mathcal{I}_V} = 0$ , directly sum up two inequalities of Theorem 3 yields

$$\begin{aligned} &\max_{\substack{i \in \mathcal{I}_A \\ \omega \in [\omega_i^d, \omega_i^c]}} \log \sigma_i(S(j\omega)) + \max_{\substack{i \in \mathcal{I}_V \\ \omega \in [\omega_i^d, \omega_i^c]}} \log \sigma_i(S(j\omega)) \\ &\geq \frac{\sum_{i \in \mathcal{I}} \left[ \omega_i^d \log \frac{1}{\alpha_i} - \frac{3c_i \omega_i^c}{2k_i} \right]}{n \max_{i \in \mathcal{I}} (\omega_i^c - \omega_i^d)} \end{aligned} \quad (14)$$

The inequality suggests that the maximum sensitivities of both phase-angle and voltage dynamics have a lower bound determined solely by the system configuration. For example, if decreasing  $\max \log \sigma_i(S(j\omega))$  for  $i \in \mathcal{I}_V$ , the phase-angle-related sensitivity will increase to satisfy the inequality.

Apart from the sensitivity breaking phenomenon, some other interesting results can also be derived from the theorem. For example, if one hopes to achieve better disturbance rejection capability by decreasing  $\alpha_i$  in the designable band  $[-\omega_i^d, \omega_i^d]$ , then the right-hand side of (13) must increase, indicating a larger sensitivity peak beyond the designable region. Meanwhile, an attempt to extend the designable frequency bandwidth  $\omega_i^d$  closer to the inherent available bandwidth  $\omega_i^c$  also leads to a larger peak of the sensitivity function. In this context, Theorem 3 lays a *fundamental limit* on the control design of coupled systems.

Now, we summarize the breaking of sensitivity conservation induced by angle-voltage coupling dynamics as follows:

**Breaking of Sensitivity Conservation**: Despite the invariant total integral of the sensitivity function, the angle-

voltage coupling reshapes the sensitivity distribution between two quantities, i.e.,  $\mathcal{A}_{\mathcal{I}_A}(S) = -\mathcal{A}_{\mathcal{I}_V}(S) \neq 0$ . The non-zero integral worsens sensitivity for one quantity while enhancing that for the other, as suggested by (13). Besides, enhancing the stability of one subsystem is at the expense of the other, as suggested by (14). For example, increasing the disturbance rejection capability of phase-angle dynamics (decreasing  $\max_{i \in \mathcal{I}_A} \log \sigma(S)$ ) leads to worse voltage dynamics (increasing  $\max_{i \in \mathcal{I}_V} \log \sigma(S)$ ) to satisfy the lower bound of their sum. More significantly, the restriction cannot be overcome under feedback control structures, which is why it is called *fundamental limit*.

Therefore, in control designs of angle-voltage coupled systems, it would be tricky to balance the stability of both quantities. The angle-voltage coupling formed by the natural power flow distribution usually worsens the stability, as shown by the following simulations. However, the proposed theory sheds new light on the coordinated control between phase-angle and voltage dynamics. Specifically, as  $\mathcal{A}_{\mathcal{I}_A}(S) = -\mathcal{A}_{\mathcal{I}_V}(S)$  holds, we can improve phase-angle/voltage dynamics through proper voltage/phase-angle controller design. This idea is called *cross-loop control* for inverters and has raised increasing concerns [2], [14]. Therefore, while setting the fundamental limit for the cross-loop controller, the proposed mechanism also provides some principles for its design. A primary example is given in Section IV-A and IV-B to show how to enhance stability by redistributing angle-voltage coupling.

#### IV. SIMULATION ANALYSIS

In all simulations of this paper, SGs and constant power loads are replaced by inverter-interfaced resources. The detailed simulation settings are provided in Appendix B of [27]. All data and codes will be open-sourced at [https://github.com/lingo01/waterbed\\_effect](https://github.com/lingo01/waterbed_effect) upon acceptance.

##### A. Analysis of Sensitivity Breaking in Single-device System

To test the proposed theory on the single-device system, we use the well-known virtual synchronous generator (VSG) control and  $Q - V$  droop control, the dynamics of which are provided in Table I. In this case, the sensitivity integral is  $\mathcal{A}_{\mathcal{I}_A}(S) = -\mathcal{A}_{\mathcal{I}_V}(S) = 0.2805$ . Since phase-angle dynamics dominate the critical eigenvalues, the coupling worsens the overall stability, as shown in Fig.3(a)(d). According to Theorem 3,  $\mathcal{A}_{\mathcal{I}_A}(S) > 0$  will enforce a stability trade-off between phase-angle and voltage subsystems and worsen the former. As confirmed in Fig.3(b), the coupling amplifies the phase-angle sensitivity peak  $\max \log \sigma = 2.0300$  at  $10^{0.521} = 3.32$  Hz, which is  $10^{2.0171-1.8246} = 1.5575$  times higher than the non-coupled case. Conversely, Fig.3(c) shows higher voltage-related sensitivity at low frequencies ( $\omega < 1$  Hz), confirming the compensation required by sensitivity conservation. The time-domain simulation verifies the result: after counting for the coupling effect, the phase-angle disturbance is suppressed as shown in Fig.3(e), while the voltage disturbance is slightly amplified as shown in Fig.3(f).

##### B. Sensitivity-Redistribution-Based Control Tuning

Despite the sensitivity conservation, one can achieve better dynamic responses by reshaping the sensitivity distribution. As

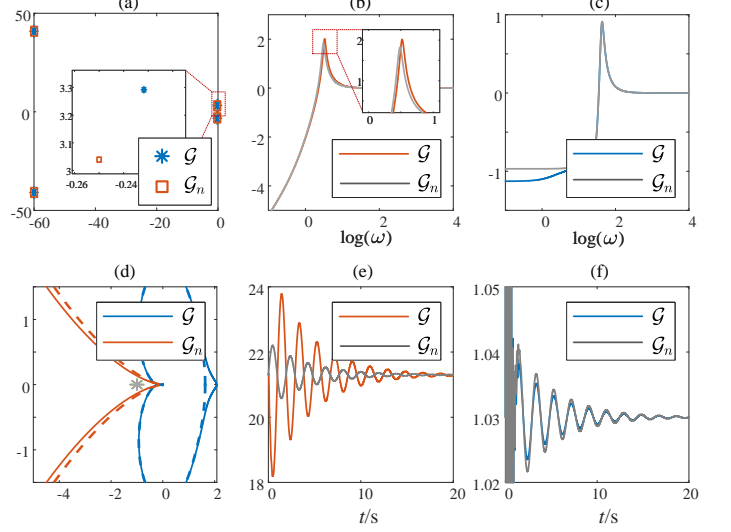


Fig. 3. Breaking of sensitivity conservation in the single-device system. (a): eigenvalues of the linearized state-space systems. (b) and (c): eigenvalues of the coupled system  $S$  and the non-coupled system  $S_n$ . The eigenvalues in (b) and (c) are induced by phase-angle and voltage dynamics, respectively. (d) generalized Nyquist curves of  $L$  and  $L_n$ . (e) and (f): time-domain simulation of phase-angle and voltage dynamics under disturbance  $\varepsilon = 0.1 \cdot [\cos(80^\circ), \sin(80^\circ)] \cdot \text{Impulse}(t)$ , where  $\text{Impulse}(t)$  is the unit impulse signal.

the angle-voltage coupling has been demonstrated to worsen the phase-angle dynamics in the above subsection, the control target is to suppress the phase-angle-induced sensitivity peak around  $10^{1\sim 2}$  Hz. Inspired by the proposed mechanism, we should decrease  $\mathcal{A}_{\mathcal{I}_A}(S)$ , or equivalently, increase  $\mathcal{A}_{\mathcal{I}_V}(S) = -\mathcal{A}_{\mathcal{I}_A}(S)$  to enhance phase-angle dynamics. Physically, it suggests that tuning either the phase-angle or voltage control parameters could enhance stability. The following analysis will verify both approaches, as we explain.

1) *Phase-angle Parameter Tuning*: A straightforward way to suppress the maximum sensitivity is to tune the phase-angle dynamics, which can be reformulated as  $\tilde{G}_{\theta P} = (1/d)/[s(s/(d/M) + 1)]$ . Specifically, we focus on tuning the phase-angle damping coefficient  $d$ . As indicated by the generalized Nyquist plot shown in Fig.3(d), increasing  $d$  has two aspect of effects: Firstly, the smaller static gain  $1/d$  pushes the eigenvalue locus away from  $(-1, 0j)$ . Secondly, the bandwidth to hold  $\log \sigma_{\mathcal{I}_A}(S(j\omega)) < 0$  as it is controlled by the frequency  $d/M$ . Both effects help to decrease the  $\mathcal{A}_{\mathcal{I}_V}(S)$  and thus are beneficial to stability. For verifications, the phase-angle damping is doubled, and the test results are shown in Fig.4(a) and (b). After the tuning, the sensitivity area  $\mathcal{A}_{\mathcal{I}_A}(S) = -\mathcal{A}_{\mathcal{I}_V}(S)$  decreases from 0.2805 to 0.2736, and the sensitivity peak  $\max \sigma(S)$  decreases from 7.5140 to 3.7777. The state-space characteristics also align with the above analysis. The critical eigenvalues move away from the imaginary axis in Fig.4(c).

2) *Voltage Parameter Tuning*: The conservation  $\mathcal{A}_{\mathcal{I}_V}(S) = -\mathcal{A}_{\mathcal{I}_A}(S)$  provides an alternative approach to enhance stability through the design of the voltage controller  $\tilde{G}_{VQ} = 1/k_q$ . By decreasing the voltage droop strength  $k_q$ , the voltage-related eigenvalues are closer to  $(-1, 0j)$  on the Nyquist plot in Fig.3(d). This leads to larger bandwidth for  $\log \sigma_{\mathcal{I}_V}(S(j\omega)) > 0$ , and finally, increase  $\mathcal{A}_{\mathcal{I}_V}(S)$ . For

verifications, we consider  $k'_q = k_q/2$ . Since the corresponding sensitivity is shifted upward, the integral  $\mathcal{A}_{\mathcal{I}_V}(S)$  is increased. Fig.4(a) and (b) show the sensitivity distribution before and after tuning. The sensitivity integral  $\mathcal{A}_{\mathcal{I}_A}(S)$  changes from 0.2805 to 0.2492, while the maximum peak  $\max \sigma(S)$  decreases from 7.5140 to 7.0358, verifying the effectiveness of tuning voltage parameters. On the contrary, voltage dynamics are slightly sacrificed on the low-frequency bandwidth due to sensitivity conservation. However, this would be acceptable as the voltage dynamics do not dominate the most critical mode. The state-space eigenvalues are depicted in Fig.4(d). After tuning, the critical eigenvalues shift away from the imaginary axis, improving the stability of the whole system. A further verification on multiple-device systems is provided in Appendix C.

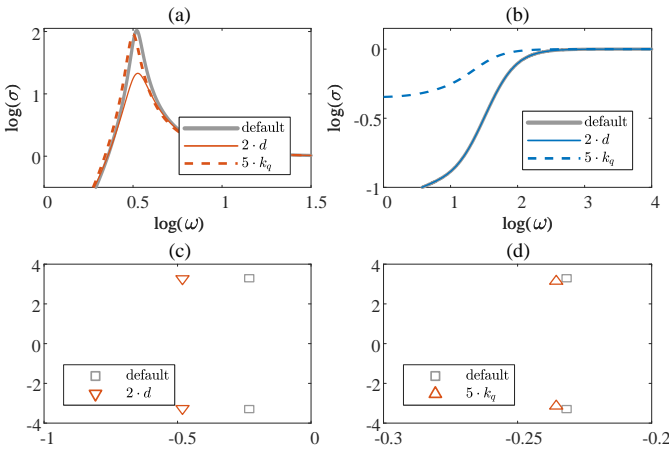


Fig. 4. Redistributing sensitivity breaking in the single-device system. (a) and (b) are the frequency distributions of phase-angle and voltage-originated sensitivity eigenvalues  $\sigma(S)$ . The gray curves, colored solid curves, and colored dashed curves represent the default, phase-angle-tuned (damping  $2 \cdot d$ ), and voltage-tuned (droop strength  $5 \cdot k_q$ ) tuned settings in order. (c) and (d) show the state-space eigenvalues before and after phase-angle and voltage tuning, respectively.

The above simple case also reveals potential pitfalls in inverter control, which we further summarize in Remark 2.

**Remark 2.** A prevalent belief in our society holds that enhancing a device's phase-angle support capability through approaches like GFM control can improve overall system stability. Furthermore, it is generally assumed that strengthening synchronization performance either has no significant impact on voltage dynamics or at least introduces no adverse effects. However, our study demonstrates contradictory conclusions. As shown in Fig.5, we enhance the synchronization performance by increasing the damping parameter  $d$  in the phase-angle control. When  $d$  becomes sufficiently large, we have  $\Delta\omega_i/\Delta P_i = s\tilde{G}_{\theta P,i}(s) \approx 1/d$ , i.e., the device operates approximately in a constant frequency state. In this scenario, Fig.5(a) confirms that the maximum phase-angle-related eigenvalue indeed decreases with increasing  $d$ . Nevertheless, while the maximum voltage-related eigenvalue only slightly increased from 1.118653, 1.118726, 1.118940 to 1.118939, their low-frequency disturbance rejection capability exhibits marked degradation as shown in Fig.5(b).

This finding carries critical implications for stability-oriented control design: when attempting to strengthen the

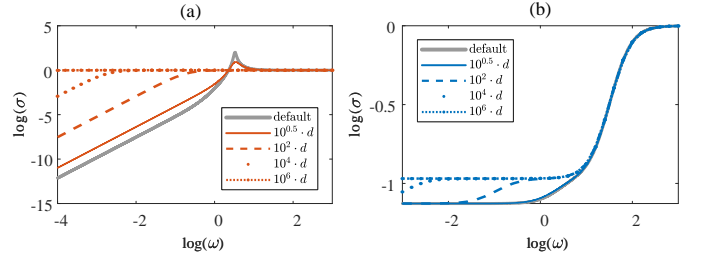


Fig. 5. Sensitivity distribution with ultra-strong phase-angle support. The phase-angle damping is scaled with  $10^0$ (default),  $10^{0.5}$ ,  $10^1$ ,  $10^4$ ,  $10^6$  times in order. (a): phase-angle-related eigenvalue. (b): voltage-related eigenvalue.

regulation of one physical quantity, its potential detrimental effects on other quantities must be carefully evaluated. Otherwise, the system might trend toward instability in other dynamic dimensions. Specifically, when enhancing synchronization performance through various GFM control strategies, particular attention should be paid to whether the corresponding voltage stability margin is compromised.

### C. Sensitivity Breaking in Multiple-device System

The test is conducted on the IEEE 14-, 30-, and 118-bus systems. Its sensitivity integral  $\mathcal{A}_{\mathcal{I}_A}(S) = -\mathcal{A}_{\mathcal{I}_V}(S) > 0$  in all cases. The positive  $\mathcal{A}_{\mathcal{I}_A}(S)$  index indicates the worsened phase-angle dynamics induced by the coupling, according to the proposed sensitivity conservation breaking. Take the IEEE 14-bus system as an example. As verified in Fig.6 and Tbl.II, the phase-angle-related sensitivity curves are steeper than the non-coupled ones, and their maximum values around 10<sup>0.5~1</sup> Hz are all increased after considering the angle-voltage coupling, i.e.,  $\max \sigma(S)/\max \sigma(S_n) = 1.2235$ . Besides, since the critical modes are more strongly related to the phase-angle dynamics, the increased sensitivity integral worsens the stability of closed-loop systems. On the contrary, the voltage-related sensitivity functions are suppressed, as shown by the lower blue solid curves compared to the blue dashed ones in Fig.6. The state-space eigenvalue analysis confirms this fact, as depicted in Fig.6(a), (d), and (g). Compared to the eigenvalues of the non-coupled system drawn in red squares, their counterparts considering the angle-voltage coupling, drawn in blue stars, move even closer to the imaginary axis, which aligns with the observations in [14].

TABLE II  
MAXIMUM SENSITIVITY VALUE FOR GFM-INTEGRATED SYSTEMS

| case     | $\frac{\mathcal{A}_{\mathcal{I}_A}}{(-\mathcal{A}_{\mathcal{I}_V})}$ | $\max \sigma(S)$ | $\max \sigma(S_n)$ | $\frac{\max \sigma(S)}{\max \sigma(S_n)}$ |
|----------|--|------------------|--------------------|---|
| IEEE 14  | 3.6739   | 9.9034           | 12.7336            | 1.2235                                    |
| IEEE 57  | 21.5448  | 51.3677          | 11.1137            | 4.6010                                    |
| IEEE 118 | 15.6626  | 88.0765          | 61.5389            | 1.4315                                    |

The simulations conducted on the other test systems provide similar results, but they are not displayed due to space limitations. The relationship between their sensitivity integrals and maximum eigenvalue is summarized in Tbl.II

Time-domain simulation results also support the above analysis, as shown in Fig.7. Disturbances with different directions  $(\Delta\theta, \Delta V) = 0.05 \cdot (\cos(\varphi)\mathbb{1}, \sin(\varphi)\mathbb{1})$  are added to study the impact of angle-voltage coupling on the dynamics. The larger

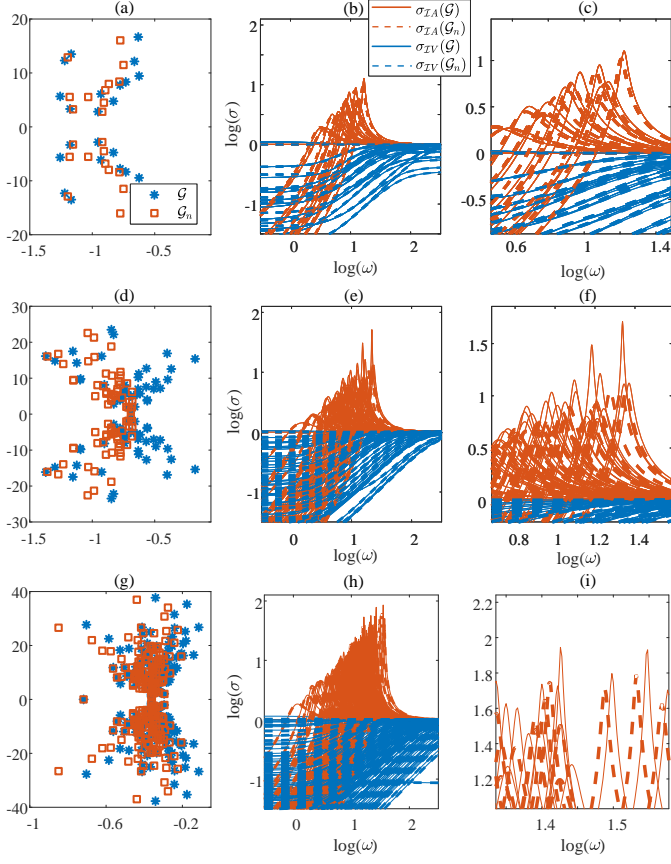


Fig. 6. Breaking of sensitivity conservation in the IEEE 14-, 57, and 118-bus systems. (a), (d) and (g): eigenvalues of the closed-loop linearized state space models for each system. (b), (e) and (h): eigenvalues of these systems. Solid and dashed lines stand for the coupled system  $S$  and the non-coupled system  $S_n$ , respectively. The orange and blue colors represent the eigenvalues induced by phase-angle and voltage dynamics, respectively. In the figure, we use  $\sigma_{\mathcal{I}_A}$  to denotes all eigenvalues  $\sigma_i$  for  $i \in \mathcal{I}_A$ , and similarly for  $\sigma_{\mathcal{I}_V}$ . (c), (f) and (i) are the zoomed-in versions of (b), (e), and (h).

$\varphi$  indicates the disturbance is more voltage-related, while a smaller one suggests the angle-related disturbance. Compared to the non-coupled counterparts in Fig. 7(a)-(c), the phase-angle dynamics, after considering the coupling effect, have more oscillation modes with larger amplitude and steady-state error, as shown in Fig. 7(d)-(f). Besides, the amplification effect of coupling to the phase-angle oscillation is more significant as the disturbance is more coupled with voltage dynamics, i.e.,  $\varphi = 45^\circ$  or  $80^\circ$  compared to  $\varphi = 10^\circ$ . On the other hand, the voltage dynamics are less influenced by the coupling, as shown in Fig. 7(g)-(l).

## V. EXTENSION TO GFM-GFL HYBRID SYSTEMS

In this section, we discuss the potential of extending the proposed method from pure GFM-integrated systems to GFM-GFL hybrid systems.

### A. Theoretical Derivation

The sets of GFM and GFL devices are respectively denoted by  $\mathcal{M}$  and  $\mathcal{L}$ , i.e.,  $\mathcal{V} = \mathcal{M} \cup \mathcal{L}$ . Due to the distinguished synchronization mechanism, GFL devices are usually modeled by differential equations from input  $[\theta, V]$  to output  $[P, Q]$ ,

opposite to GFM devices. For  $i \in \mathcal{L}$ , a classical GFL model [33], [34] can be written as

$$\begin{aligned} -\frac{\Delta P_i}{\Delta \theta_i} &= \frac{d_{p,i}}{\tau_{p,i}s + 1} \frac{s(K_{p,i}V_i^*s + K_{i,i}V^*)}{s^2 + K_{p,i}V_i^*s + K_{i,i}V^*} \stackrel{\text{def}}{=} G_{P\theta,i} \\ -\frac{\Delta Q_i}{\Delta V_i} &= \frac{d_{q,i}}{\tau_{q,i}s + 1} \stackrel{\text{def}}{=} G_{QV,i} \end{aligned} \quad (15)$$

where  $K_p$  and  $K_i$  are PI parameters of the phase-lock loop (PLL), and  $d_p$  and  $d_q$  are  $f - P$  and  $V - Q$  droop gains, respectively. For brevity, we denote  $G_{P\theta}(s) = \text{diag}(G_{P\theta,1}, G_{P\theta,2}, \dots, G_{P\theta,n})$  and similar for  $G_{QV}(s)$ . Then, the dynamics of GFL devices can be represented by  $G_{\mathcal{L}} = \text{diag}(G_{P\theta}, G_{QV})$ .

The GFL devices cannot be directly written in the form of (5) as the inverse input-output relationship might lead to non-causality of transfer functions, i.e., the higher numerator's order of  $G_{P\theta}^{-1}$  and  $G_{QV}^{-1}$ . Alternatively, we turn to treat the GFL devices as a part of the network, as shown in Fig. 8.

Then the expression of the equivalent network  $\tilde{H}_{\text{net}}$  is derived. The original network coupling  $H_{\text{net}}$  for hybrid systems can be block-wisely written as

$$\begin{bmatrix} \Delta P_{\mathcal{M}} \\ \Delta P_{\mathcal{L}} \\ \Delta Q_{\mathcal{M}} \\ \Delta Q_{\mathcal{L}} \end{bmatrix} = \begin{bmatrix} H_{P\theta,\mathcal{M}\mathcal{M}} & H_{P\theta,\mathcal{M}\mathcal{L}} & H_{P\mathcal{V},\mathcal{M}\mathcal{M}} & H_{P\mathcal{V},\mathcal{M}\mathcal{L}} \\ H_{P\theta,\mathcal{L}\mathcal{M}} & H_{P\theta,\mathcal{L}\mathcal{L}} & H_{P\mathcal{V},\mathcal{L}\mathcal{M}} & H_{P\mathcal{V},\mathcal{L}\mathcal{L}} \\ H_{Q\theta,\mathcal{M}\mathcal{M}} & H_{Q\theta,\mathcal{M}\mathcal{L}} & H_{Q\mathcal{V},\mathcal{M}\mathcal{M}} & H_{Q\mathcal{V},\mathcal{M}\mathcal{L}} \\ H_{Q\theta,\mathcal{L}\mathcal{M}} & H_{Q\theta,\mathcal{L}\mathcal{L}} & H_{Q\mathcal{V},\mathcal{L}\mathcal{M}} & H_{Q\mathcal{V},\mathcal{L}\mathcal{L}} \end{bmatrix} \begin{bmatrix} \Delta \theta_{\mathcal{M}} \\ \Delta \theta_{\mathcal{L}} \\ \Delta V_{\mathcal{M}} \\ \Delta V_{\mathcal{L}} \end{bmatrix} \quad (16)$$

where the submatrices denote the corresponding positions in the network coupling matrix. For example,  $H_{P\theta,\mathcal{M}\mathcal{L}} = [H_{P\theta,ij}]$  where  $i \in \mathcal{M}$  and  $j \in \mathcal{L}$ . Then, following a matrix transformation method, we can obtain its equivalent form from inputs  $[\Delta \theta_{\mathcal{M}}^T, \Delta P_{\mathcal{L}}^T, \Delta V_{\mathcal{M}}^T, \Delta Q_{\mathcal{L}}^T]^T$  to outputs  $[\Delta P_{\mathcal{M}}^T, \Delta \theta_{\mathcal{L}}^T, \Delta Q_{\mathcal{M}}^T, \Delta V_{\mathcal{L}}^T]^T$ .

Meanwhile, the dynamics of GFM devices satisfy  $-\Delta P_{\mathcal{L}} = G_{P\theta} \Delta \theta_{\mathcal{L}}$  and  $-\Delta Q_{\mathcal{L}} = G_{QV} \Delta V_{\mathcal{L}}$ . Combining both above equations and eliminating GFL-related variables using the standard Gaussian elimination method yields

$$[\Delta P_{\mathcal{M}}^T \quad \Delta Q_{\mathcal{M}}^T]^T = \tilde{H}_{\text{net}}(s) [\Delta \theta_{\mathcal{M}}^T \quad \Delta V_{\mathcal{M}}^T]^T \quad (17)$$

where the equivalent network coupling is provided by

$$\tilde{H}_{\text{net}}(s) = H_{\mathcal{M}\mathcal{M}} - H_{\mathcal{M}\mathcal{L}}[G_{\mathcal{L}} + H_{\mathcal{L}\mathcal{L}}(s)]^{-1}H_{\mathcal{L}\mathcal{M}} \quad (18)$$

The submatrices are defined by the blocks in (16). For example,  $H_{\mathcal{M}\mathcal{L}}$  is used to denote the following matrix.

$$H_{\mathcal{M}\mathcal{L}} = \begin{bmatrix} H_{P\theta,\mathcal{M}\mathcal{L}} & H_{P\mathcal{V},\mathcal{M}\mathcal{L}} \\ H_{Q\theta,\mathcal{M}\mathcal{L}} & H_{Q\mathcal{V},\mathcal{M}\mathcal{L}} \end{bmatrix} \quad (19)$$

The non-coupled network coupling matrix  $\tilde{H}_{\text{net}}^{(n)}$  can be similarly obtained through reduction.

Distinguished from the constant matrix  $H_{\text{net}}$ , the equivalent network  $\tilde{H}_{\text{net}}(s)$  is a transfer function as the GFL dynamics  $G_{\mathcal{L}}(s)$  are involved. It is noted that the conditions of Theorem 2 and 3 still hold for the equivalent system as  $\tilde{H}_{\text{net}}$  generally do not provide relative degree (see the inverse structure in (18)). Therefore, through the substitution from  $H_{\text{net}}$  to  $\tilde{H}_{\text{net}}$ , the analysis methodology developed for pure GFM-integrated systems still works on GFM-GFL hybrid systems by combining (5) and (17).

After obtaining the  $\tilde{H}_{\text{net}}(s)$  and  $\tilde{H}_{\text{net}}^{(n)}(s)$ , the sensitivity transfer matrices can be similarly derived. Here we note that the replaced sensitivity still reflects the internal stability of the feedback system. In fact, if adding the condition " $\tilde{H}_{\text{net}}(s)$  is

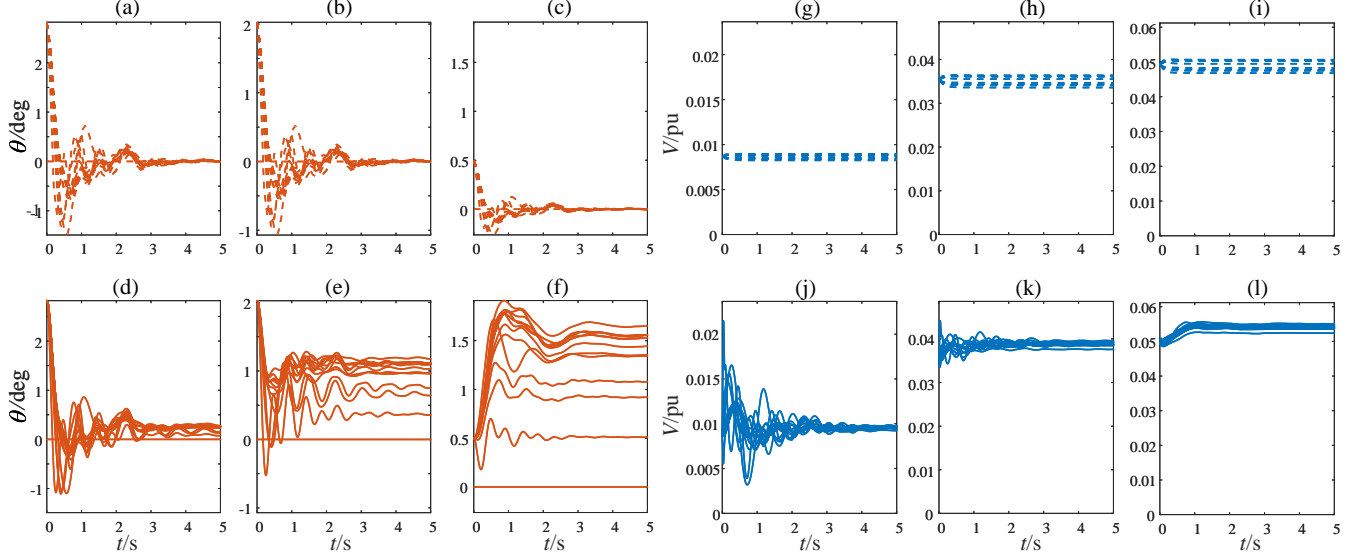


Fig. 7. Dynamics of the IEEE 14-bus system under the phase-angle and voltage disturbances. Each  $i$ -th device is disturbed with  $\Delta\theta_i = 0.05 \cdot \cos(\varphi) \cdot \text{Step}(t)$  and  $\Delta V_i = 0.05 \cdot \sin(\varphi) \cdot \text{Step}(t)$  except the reference bus, where  $\varphi$  stand for the disturbance direction and  $\text{Step}(t)$  is the unit step signal. (a), (b) and (c): phase-angle dynamics of the non-coupled system  $\mathcal{G}_n$  under  $\varphi = 10^\circ$ ,  $45^\circ$ , and  $80^\circ$ . (d), (e) and (f): phase-angle dynamics of the coupled system  $\mathcal{G}$  under the same disturbance. (g), (h) and (i) show the non-coupled voltage dynamics, while (j), (k), and (l) depict those of the coupled system, similar to (a)-(f).

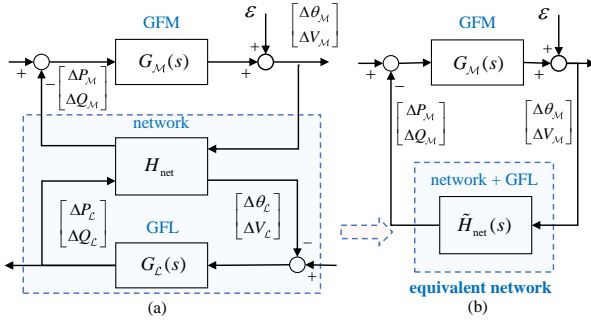


Fig. 8. Network equivalence for hybrid GFM-GFL integrated power systems. (a): model of hybrid GFM-GFL systems. (b): formulation of the equivalent dynamic network by merging the original network and GFL devices.

stable” in the proof of Theorem 1, all following statements of this Theorem still hold.

### B. Simulation Verification

Still takes the above benchmarks to test the proposed theory on GFM-GFL hybrid systems. All generators are replaced with GFM inverters, and all loads are replaced with GFL inverters. Their sensitivity integrals are depicted in Tbl.III. For the IEEE 14-, 57-, and 118-bus systems,  $\mathcal{A}_{\mathcal{I}_A} > 0$ , indicating that the coupling’s impact worsens the phase-angle dynamics, as predicted by our theory. Fig.9 shows their sensitivity distribution. Similar to Fig.6, the phase-angle-related sensitivities (solid curves) are enlarged compared to the non-coupled systems (dashed curves). Besides, the maximum sensitivity increases as listed in Tbl.III since it originates from the phase-angle dynamics. On the contrary, the voltage-related sensitivity is suppressed, as shown by the lower blue solid curves compared to the blue dashed ones.

TABLE III  
SENSITIVITY DISTRIBUTION OF GFM-GFL-INTEGRATED SYSTEMS

| case name | $\mathcal{A}_{\mathcal{I}_A}$<br>$(-\mathcal{A}_{\mathcal{I}_V})$ | max $\sigma(S)$ | max $\sigma(S_n)$ | $\frac{\max \sigma(S)}{\max \sigma(S_n)}$ |
|-----------|---|-----------------|-------------------|---|
| IEEE 14   | 0.8214  | 4.8892          | 4.1752            | 1.1710                                    |
| IEEE 57   | 2.5103  | 5.8348          | 5.1632            | 1.1301                                    |
| IEEE 118  | 27.6237   | 7.6169          | 6.1517            | 1.2382                                    |

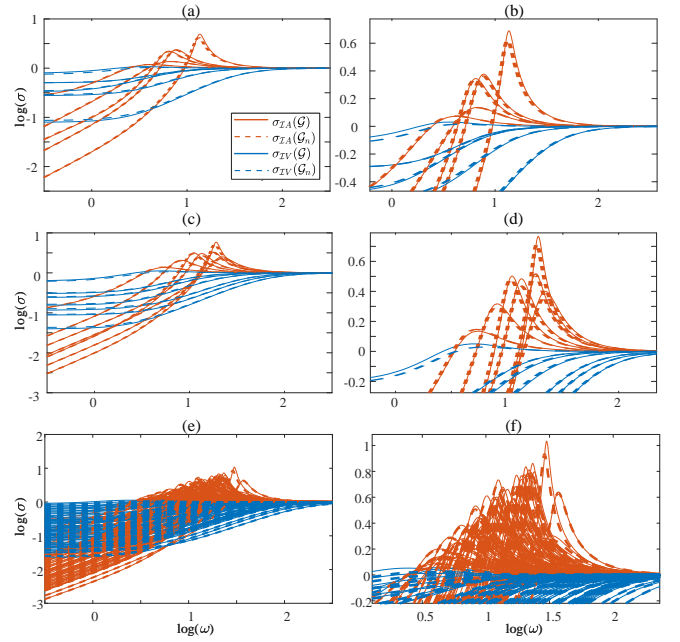


Fig. 9. Breaking of sensitivity conservation in the IEEE 14-, 57-, and 118-bus systems. (a), (c) and (e): sensitivity eigenvalues. Solid and dashed lines represent the coupled system  $S$  and the non-coupled system  $S_n$ , respectively. (b), (d) and (f) are the zoomed-in versions of (a), (c) and (e).

## VI. CONCLUSION

This paper provides a novel frequency-domain perspective to understand the mechanism of angle-voltage coupling's impact on system dynamics. While the sum of sensitivity integrals is conservative, the coupling redistributes them between phase-angle and voltage dynamics, thus worsening one quantity's dynamics while improving the other's. Therefore, the stability of the coupled system is usually weakened by the waterbed effect. The sensitivity conservation and breaking laws cannot be directly bypassed by any controllers with a generic feedback structure, as shown in Fig.1. In other words, this phenomenon should be treated as a fundamental limit of coupled power systems, as recognized for the first time in the angle-voltage coupling dynamics.

However, despite the conservative total sensitivity, the proposed theory also inspires us that it is still possible to improve the weakest dynamics by reasonably transferring sensitivity between different frequencies, devices, or between phase-angle and voltage dynamics. This paper suggests that tuning the parameters based on the proposed theory will enhance the stability. Besides, this design should be comprehensively evaluated, as strengthening the synchronization capability might also lead to detrimental effects on voltage dynamics, revealed by our studies. Therefore, the sensitivity conservation and its breaking laws should be carefully treated as one design principle for system controls. Apart from tuning the existing controllers as presented above, the proper cross-loop controls [14] might also benefit the redistribution of sensitivity, the systematic design of which is our future research direction.

## REFERENCES

- [1] N. Hatzigyriou, J. Milanovic, C. Rahmann, V. Ajjarapu, C. Canizares, I. Erlich, D. Hill, I. Hiskens *et al.*, "Definition and classification of power system stability - revisited & extended," *IEEE Transactions on Power Systems*, vol. 36, no. 4, pp. 3271–3281, 2021.
- [2] F. Zhao, X. Wang, and T. Zhu, "Power dynamic decoupling control of grid-forming converter in stiff grid," *IEEE Transactions on Power Electronics*, vol. 37, no. 8, pp. 9073–9088, 2022.
- [3] P. Yang, F. Liu, Z. Wang, S. Wu, and H. Mao, "Spectral analysis of network coupling on power system synchronization with varying phases and voltages," in *2020 Chinese Control And Decision Conference (CCDC)*. Hefei, China: IEEE, 2020, pp. 880–885.
- [4] L. Zhang and H.-P. Nee, "Multivariable feedback design of vsc-hvdc connected to weak ac systems," in *2009 IEEE Bucharest PowerTech*, 2009, pp. 1–8.
- [5] Z. Gong, C. Liu, F. F. Da Silva, Y. Gui, and C. L. Bak, "Fast Coordinated Power Control for Improving Inertial and Voltage Support Capability of Battery Energy Storage Systems," *CSEE Journal of Power and Energy Systems*, vol. 11, no. 1, pp. 280–295, 2025.
- [6] L. Fan, Z. Wang, and Z. Miao, "Large angle deviation in grid-following ibrs upon grid voltage dip," *IEEE Transactions on Energy Conversion*, vol. 39, no. 1, pp. 368–378, 2024.
- [7] W. Si, W. Li, N. Tashakor, and J. Fang, "Joint transient angle and voltage stability analysis and enhancement of grid-forming converters," *IEEE Transactions on Industrial Electronics*, pp. 1–12, 2024.
- [8] M. Li, Y. Wang, W. Hu, S. Shu, P. Yu, Z. Zhang, and F. Blaabjerg, "Unified modeling and analysis of dynamic power coupling for grid-forming converters," *IEEE Transactions on Power Electronics*, 2021.
- [9] J. Schiffer, R. Ortega, A. Astolfi, J. Raisch, and T. Sezi, "Conditions for stability of droop-controlled inverter-based microgrids," *Automatica*, vol. 50, no. 10, pp. 2457–2469, 2014.
- [10] K. Sharafutdinov, L. Rydin Gorjão, M. Matthiae, T. Faulwasser, and D. Withaut, "Rotor-angle versus voltage instability in the third-order model for synchronous generators," *Chaos*, vol. 28, no. 3, 2018.
- [11] K. De Brabandere, B. Bolsens, J. Van den Keybus, A. Woyte, J. Driesen, and R. Belmans, "A voltage and frequency droop control method for parallel inverters," *IEEE Transactions on Power Electronics*, vol. 22, no. 4, pp. 1107–1115, 2007.
- [12] W. Zhong, G. Tzounas, and F. Milano, "Improving the power system dynamic response through a combined voltage-frequency control of distributed energy resources," *IEEE Transactions on Power Systems*, vol. 37, no. 6, pp. 4375–4384, 2022.
- [13] P. Yang, F. Liu, Z. Wang, and C. Shen, "Distributed stability conditions for power systems with heterogeneous nonlinear bus dynamics," *IEEE Transactions on Power Systems*, vol. 35, no. 3, pp. 2313–2324, 2020.
- [14] X. Peng, C. Fu, P. Yang, X. Ru, and F. Liu, "Impact of angle-voltage coupling on small-signal stability of power systems: A damping perspective," *IEEE Transactions on Circuits and Systems I: Regular Papers*, 2025.
- [15] F. Zhao, T. Zhu, Z. Li, and X. Wang, "Low-frequency resonances in grid-forming converters: Causes and damping control," *IEEE Transactions on Power Electronics*, vol. 39, no. 11, pp. 14430–14447, 2024.
- [16] T. Wen, D. Zhu, X. Zou, B. Jiang, L. Peng, and Y. Kang, "Power coupling mechanism analysis and improved decoupling control for virtual synchronous generator," *IEEE Transactions on Power Electronics*, vol. 36, no. 3, pp. 3028–3041, 2021.
- [17] Q. Ma, Y. Min, Y. Gong, and K. Liang, "Effect of grid-following vsc on terminal frequency," *IEEE Transactions on Power Systems*, vol. 38, no. 2, 2023.
- [18] X. Wang, Y. W. Li, F. Blaabjerg, and P. C. Loh, "Virtual-Impedance-Based Control for Voltage-Source and Current-Source Converters," *IEEE Transactions on Power Electronics*, vol. 30, no. 12, pp. 7019–7037, 2015.
- [19] Y. Li, Y. Gu, and T. C. Green, "Revisiting grid-forming and grid-following inverters: A duality theory," *IEEE Transactions on Power Systems*, vol. 37, no. 6, pp. 4541–4554, 2022.
- [20] S. Fu, Y. Sun, J. Lin, S. Chen, and M. Su, " $P/Q-\omega/V$  admittance modeling and oscillation analysis for multi-vsg grid-connected system," *IEEE Transactions on Power Systems*, vol. 38, no. 6, 2023.
- [21] S. Fu, Y. Sun, X. Hou, S. Chen, G. Shi, and M. Su, "A general  $[p\ q]-[\omega\ v]$  model of hybrid gfm/gfl multi-vsc systems: Power oscillation analysis and suppression method," *IEEE Journal of Emerging and Selected Topics in Industrial Electronics*, vol. 5, no. 4, 2024.
- [22] H. Bode, *Network Analysis and Feedback Amplifier Design*. New York: Van Nostrand, 1945.
- [23] G. Stein, "Respect the unstable," *IEEE Control Systems Magazine*, vol. 23, no. 4, pp. 12–25, 2003.
- [24] J. Chen, "Sensitivity integral relations and design trade-offs in linear multivariable feedback systems," *IEEE Transactions on Automatic Control*, vol. 40, no. 10, pp. 1700–1716, 1995.
- [25] M. M. Seron, J. H. Braslavsky, and G. C. Goodwin, *Fundamental Limitations in Filtering and Control*, ser. Communications and Control Engineering. London: Springer London, 1997.
- [26] M. H. Ravanji, D. B. Rathnayake, M. Z. Mansour, and B. Bahrami, "Impact of Voltage-Loop Feedforward Terms on the Stability of Grid-Forming Inverters and Remedial Actions," *IEEE Transactions on Energy Conversion*, vol. 38, no. 3, pp. 1554–1565, 2023.
- [27] X. Peng, C. Fu, Z. Li, P. Yang, Z. Wang, and F. Liu, "Supplementary materials for a fundamental limit in angle-voltage coupling dynamics: Sensitivity conservation and breaking," [https://github.com/lingo01/waterbed\\_effect](https://github.com/lingo01/waterbed_effect), 2025.
- [28] K. Zhou and J. C. Doyle, *Essentials of Robust Control*. Prentice hall Upper Saddle River, NJ, 1998, vol. 104.
- [29] X. Peng, Z. Li, K. Luo, T. Wang, S. Ma, and F. Liu, "Angle-voltage coupling can induce fundamental limits on voltage stability," in *Advanced Electrical and Energy Systems Conference (in press)*, 2025.
- [30] Z. Xin, X. Wang, P. C. Loh, and F. Blaabjerg, "Grid-current-feedback control for LCL-filtered grid converters with enhanced stability," *IEEE Transactions on Power Electronics*, vol. 32, no. 4, pp. 3216–3228, 2017.
- [31] S. Dong, A. Hoke, B. Wang, L. Ding, X. Lu, C. J. Kruse, B. W. Rockwell, and J. Tan, "A twin circuit theory-based framework for oscillation event analysis in inverter-dominated power systems with case study for kauai's system," *IEEE Transactions on Circuits and Systems I: Regular Papers*, pp. 1–14, 2025.
- [32] A. Emami-Naeini and D. de Roover, "Bode's Sensitivity Integral Constraints: The Waterbed Effect Revisited," 2019.
- [33] L. Huang, H. Xin, W. Dong, and F. Dörfle, "Impacts of grid structure on PLL-synchronization stability of converter-integrated power systems," *IFAC-PapersOnLine*, vol. 55, no. 13, pp. 264–269, 2022.
- [34] P. Yang, "Augmented synchronization based stability theory and its distributed analytics of power systems," Ph.D. dissertation, Tsinghua University, Beijing, 2022.
- [35] Y. Gu and T. C. Green, "Power system stability with a high penetration of inverter-based resources," *Proceedings of the IEEE*, vol. 111, no. 7, pp. 832–853, 2023.

## APPENDIX A PROOF OF THEOREMS

*Proof of Theorem 1.* The stability of the left-upper matrix of (7) equals to that of  $(I + GH_{\text{net}})^{-1} = S(s)$ . Besides, as the stability of  $G(s)$  and no pole-zero cancellation have been assumed in the conditions,  $(I + GH_{\text{net}})^{-1}G$  is stable if and only if  $S(s)$  is stable. Hence, we bridge the stability of the right-upper matrix of (7) with that of  $S(s)$ . Finally, consider the matrix identity  $(I + H_{\text{net}}G)^{-1}H_{\text{net}} = H_{\text{net}}(I + GH_{\text{net}})^{-1} = H_{\text{net}}S$ . It directly links the two lower matrices of (7) with  $S(s)$ . Similarly, as  $H_{\text{net}}$  is constant, they are stable if and only if  $S(s)$  is stable. Therefore, the above analysis yields that the stability of the transfer matrix (7) is equivalent to that of the sensitivity  $S(s)$ .  $\square$

*Proof of Theorem 2.* The result can be viewed as a corollary of the main theorem in [24], a more systematic statement of which can be found in [25, Theorem 4.2.2], which says that under the given conditions, each singular value of the sensitivity matrix satisfies

$$\int_0^\infty \log \delta_i(S(j\omega)) d\omega = \frac{1}{2} \iint_{\bar{C}+} x \nabla^2 \log \delta_i(S(x+jy)) dx dy \quad (20)$$

where  $\delta$  denotes the singular value and  $\bar{C}+$  is the closure of the open-right-half plane. Then, sum all singular values, and we obtain

$$\sum_{i=1}^{2n} \int_0^\infty \log \delta_i(S(j\omega)) d\omega = \frac{1}{2} \iint_{\bar{C}+} x \nabla^2 \log \det(S(x+jy)) dx dy \quad (21)$$

As the conditions of the theorem are satisfied,  $\det(S)$  is analytic on  $\bar{C}+$ , otherwise, the closed-loop transfer function is unstable. Then  $\log \det(S)$  is also analytic on  $\bar{C}+$ . Hence, we obtain zero for the equation according to the Cauchy-Goursat theorem. Finally, the proof will be completed by noticing  $\sum \log \delta_i(S(j\omega)) = \log \det(S(j\omega)) = \sum \log \sigma_i(S(j\omega))$  holds for any  $\omega \geq 0$ .  $\square$

*Proof of Theorem 3.* Due to the symmetry of phase-angle and voltage dynamics, we denote  $\mathcal{I}_*$  for either  $\mathcal{I}_A$  or  $\mathcal{I}_V$  in this proof. The integral of any  $i$ -th sensitivity eigenvalue ( $i \in \mathcal{I}_*$ ) can be split into three terms written as

$$\begin{aligned} & \int_0^\infty \log \sigma_i(S(j\omega)) d\omega = \\ & \left( \int_0^{\omega_i^d} + \int_{\omega_i^d}^{\omega_i^c} + \int_{\omega_i^c}^\infty \right) \log \sigma_i(S(j\omega)) d\omega \end{aligned} \quad (22)$$

The first term can be bounded by  $\textcircled{1} \leq \omega_i^d \log \alpha_i$ . The second and third terms respectively satisfy

$$\int_{\omega_i^d}^{\omega_i^c} \log \sigma_i(S(j\omega)) d\omega \leq \max_{r \in \mathcal{I}_*} (\omega_r^c - \omega_r^d) \max_{\substack{i \in \mathcal{I}_* \\ \omega \in [\omega_i^d, \omega_i^c]}} \log \sigma_r(S(j\omega)) \quad (23)$$

$$\int_{\omega_i^c}^\infty \log \sigma_i(S(j\omega)) d\omega \leq \int_{\omega_i^c}^\infty |\log(1 + \sigma_i(L(j\omega)))| d\omega \quad (24)$$

To examine the effect of the third term, we use the following fact, proof of which can be found in [25, Example A.8.6].

$$|\log(1 + s)| \leq 3|s|/2, |s| < 1/2 \quad (25)$$

As  $\sigma_i(L(j\omega)) \leq e_i/\omega^{k_i+1} \leq c_i < 1/2$  for  $\forall \omega \in [\omega_i^c, \infty)$  has been assumed in the condition, the above fact implies

$$\begin{aligned} & \int_{\omega_i^c}^\infty \log \sigma_i(S(j\omega)) d\omega \leq \frac{3}{2} \int_{\omega_i^c}^\infty \log \sigma_i(L(j\omega)) d\omega \\ & \leq \frac{3}{2} \int_{\omega_i^c}^\infty \frac{e_i}{\omega^{k_i+1}} d\omega = \frac{3e_i}{2k_i(\omega_i^c)^{k_i}} \leq \frac{3c_i\omega_i^c}{2k_i} \end{aligned} \quad (26)$$

Then, adding together all eigenvalues within the indicator set  $\mathcal{I}_*$  and using the above bounds will complete the proof.  $\square$

Before ending the section, we note that the bound provided in Theorem 3 can be squeezed if additional information regarding the system is given. For example, for the phase-angle dynamics with VSG control, we already know the phase-angle related eigenvalue  $\log(\sigma_{\mathcal{I}_A}) \rightarrow -\infty$  as  $\log(\omega) \rightarrow -\infty$ . Therefore, the restriction on the designable frequency band can be more precisely described, says  $\log(\sigma_i(S(j\omega))) \leq \beta_i \log(\omega) + \gamma_i, \forall i \in \mathcal{I}_A, \omega \in [0, \omega_i^d]$ , where  $\beta_i$  and  $\gamma_i$  are given constants. Based on these restrictions, a better approximation than (13) can be obtained. However, it is noted that the provided theorem takes advantage of a uniform description for any type of device dynamics.

## APPENDIX B SIMULATION SETTINGS

All data and codes will be open-sourced at [https://github.com/lingo01/waterbed\\_effect](https://github.com/lingo01/waterbed_effect) upon acceptance.

### A. GFM-Integrated Single-device System

The equilibrium of the device is set as  $(\theta_s, V_s) = (21.3^\circ, 1.03)$  while the infinite bus satisfies  $(\theta_0, V_0) = (0^\circ, 1)$ . The GFM devices take the strategies of VSG and  $Q-V$  droop controls. The dynamics are provided in Tbl.I. The parameters of the network and device are  $R + jX = 0.2 + j0.3$  and  $(M, d, T_{il}, \tau, k_q^{-1}) = (0.3, 0.15, 0.01, 0.05, 0.8)$ .

### B. GFM-Integrated Multiple-device Systems

In the simulations, all SGs and constant power loads are replaced by GFM devices. The network topology and power flow data are borrowed from the MATPOWER standard dataset. The GFM devices take the strategies of VSG (or  $P-f$  droop with low-pass power measurement filters) and  $Q-V$  droop controls. The dynamics are provided in Tbl.I. Parameters  $(M, d, T_{il}, \tau, k_q^{-1})$  are selected from normal distribution  $\mathcal{N}(0.3, 0.1^2)$ ,  $\mathcal{N}(0.8, 0.1^2)$ ,  $\mathcal{N}(0.02, 0.002^2)$ ,  $\mathcal{N}(0.3, 0.1^2)$  and  $\mathcal{N}(0.8, 0.2^2)$ . Parameter settings refer to [13], [14].

### C. Hybrid GFM-GFL Integrated Multiple-device Systems

All generators are replaced with GFM inverters, and all loads are replaced with GFL inverters. The network topology, power flow data, and GFM devices are set with the same method as above pure GFM-integrated systems, except for strengthened  $k_q^{-1} \sim \mathcal{N}(0.2, 0.05^2)$  to guarantee the system stability. As for the GFM devices, their dynamics are provided by (15). The GFL parameters  $(K_i, K_p, \tau_p, \tau_q, d_p, d_q)$  are selected from  $\mathcal{N}(590, 30^2)$ ,  $\mathcal{N}(34, 5^2)$ ,  $\mathcal{N}(1.0, 0.2^2)$ ,  $\mathcal{N}(1.0, 0.2^2)$ ,  $\mathcal{N}(1.5, 0.3^2)$ ,  $\mathcal{N}(1.5, 0.3^2)$ , which refer to [34].

#### D. Electromagnetic Dynamics

In this paper, we consider the electromagnetic control loops of inverters as shown in Fig.10.

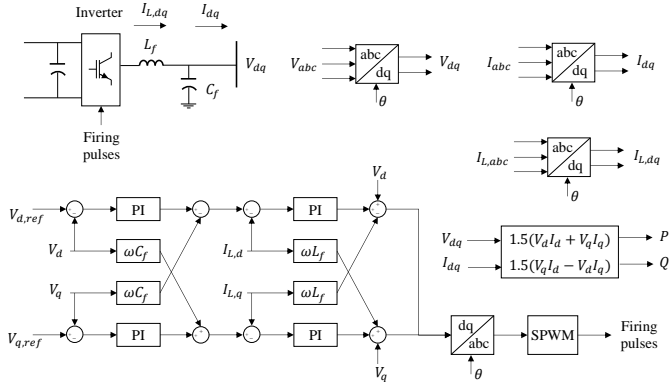


Fig. 10. Electromagnetic control loops of inverters.

As we focus on the transmission grid stability, the timescale of the current loop is much faster than the voltage loop and the synchronous dynamics of the system [35]. Therefore, the current loop dynamics can be approximated by  $G_{cc} \approx 1$ . Then, the voltage loops commonly use the PI controllers, i.e.,

$$G_{vc} = K_{vp} + \frac{K_{vi}}{s} \quad (27)$$

where  $K_{vp}$  and  $K_{vi}$  are the PI parameters of voltage loops. Then, the lag effect of electromagnetic loops can be expressed as [26]:

$$\frac{\Delta V_d(s)}{\Delta V_{dref}(s)} = \frac{\Delta V_q(s)}{\Delta V_{qref}(s)} = \frac{1}{1 + \frac{C_f s}{G_{vc} G_{cc}}} = \frac{K_{vp}s + K_{vi}}{C_f s^2 + K_{vp}s + K_{vi}} \quad (28)$$

where  $C_f$  is the LCL filter capacitor. The reference voltage  $V_{dref}$  is the output signal of  $\tilde{G}_{VQ}$  and  $V_{dref}$  is usually set as zero. Therefore, it holds that:

$$-\frac{\Delta V}{\Delta Q} = -\frac{\Delta V_d}{\Delta V_{dref}} \cdot \frac{\Delta V_{dref}}{\Delta Q} = \frac{K_{vp}s + K_{vi}}{C_f s^2 + K_{vp}s + K_{vi}} \cdot \tilde{G}_{VQ} \quad (29)$$

In other words, the lag effect of electromagnetic transients is:

$$G_{lag} = \frac{K_{vp}s + K_{vi}}{C_f s^2 + K_{vp}s + K_{vi}} \quad (30)$$

Alternatively, if considering the time delay induced by the power measurement filter, it can be written as:

$$G_{lag} = \frac{1}{T_{il} + 1} \quad (31)$$

Throughout the simulation, we adopt  $K_{vp} = 0.5$ ,  $K_{vi} = 5$ ,  $C_f = 1.59155 \times 10^{-6}$  and  $T_{il} = 0.02$ .

#### APPENDIX C SUPPLEMENTARY SIMULATION RESULTS OF PARAMETER TUNING IN MULTIPLE-DEVICE SYSTEMS

Similar to Section IV-B, we can redistribute the sensitivity to achieve better dynamic responses in multiple-device systems. Take the IEEE 14-bus system in Fig.6(a)-(c) as an example, the angle-voltage coupling of which has been demonstrated to worsen the phase-angle dynamics. Therefore, the control

target is to suppress the phase-angle-induced sensitivity peak around  $10^{0.5 \sim 1}$  Hz. According to the proposed mechanism, we should decrease  $\mathcal{A}_{\mathcal{I}_A}(S)$ , or equivalently, increase  $\mathcal{A}_{\mathcal{I}_V}(S) = -\mathcal{A}_{\mathcal{I}_A}(S)$ .

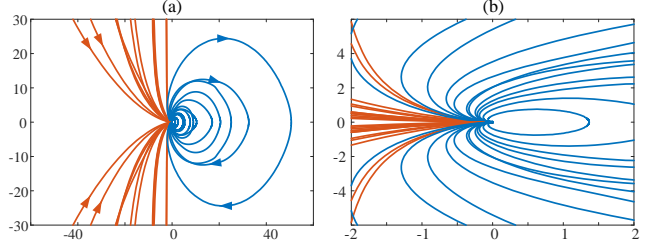


Fig. 11. Generalized Nyquist plot of the open-loop transfer function  $L(s)$  of the IEEE 14-bus system, where orange and blue curves represent phase-angle-related and voltage-related eigenvalues. (b) is its zoomed-in version.

1) *Phase-angle Parameter Tuning*: A straightforward way to suppress the maximum sensitivity is to tune the phase-angle control parameters. Similar to Section IV-B, the analysis of its generalized Nyquist plot suggests that increasing the damping  $d$  benefits for reducing  $\mathcal{A}_{\mathcal{I}_A}$  and thus enhances the stability. Specifically, the homotopy procedure as shown in [29] enables us to identify the device responsible for the maximum eigenvalue. In this case, it is the 4th inverter.

For verification, the phase-angle damping of the 4th inverter is doubled, and the test results are shown in Fig.12. After the tuning, the sensitivity area  $\mathcal{A}_{\mathcal{I}_A}(S) = -\mathcal{A}_{\mathcal{I}_V}(S)$  decreases from 4.0493 to 4.0291 (do not change much), and the sensitivity peak max  $\sigma(S)$  significantly decreases from 13.3414 to 9.3160. Specifically, the original maximum sensitivity significantly drops down from  $\log(\sigma_6) = 1.1252$  to 0.8636 and is no longer the maximum one, as highlighted by the yellow square in Fig.12(b). The time-domain characteristics also align with the above analysis. The state-space eigenvalues move away from the imaginary axis in Fig.12(a). Besides, the simulations in Fig.12(c) show that the reduced phase-angle oscillation amplitudes (orange curves) compared to the default system (gray curves), suggesting the enhancement of phase-angle dynamics. On the contrary, the voltage dynamics rarely change as depicted in Fig.12(d).

2) *Voltage Parameter Tuning*: Similar to the Single-device case, we still take  $k'_q = k_q/2$  as an example. Since the corresponding sensitivity is shifted upward, the integral  $\mathcal{A}_{\mathcal{I}_V}(S)$  is increased. Fig.13(b) shows the maximum sensitivity before and after parameter tuning. The sensitivity integral  $\mathcal{A}_{\mathcal{I}_A}(S)$  changes from 4.0493 to 2.5282, while the maximum peak max  $\sigma(S)$  decreases from 13.3414 to 12.2321, which shows the effectiveness of tuning parameters based on the proposed theory. On the contrary, the voltage dynamics are slightly sacrificed, and the maximum voltage-related sensitivity is increased, due to sensitivity conservation. The changes of both phase-angle-related and voltage-related maximum sensitivities are highlighted in yellow squares in Fig.13(b). Besides, the larger sensitivity in the low-frequency band also leads to larger steady-state errors under disturbances. However, this would be acceptable as the voltage dynamics do not dominate the most critical mode.

The state-space eigenvalue distributions before and after tuning are depicted in Fig.13(a). The critical eigenvalues shift away from the imaginary axis after tuning, thus improving the

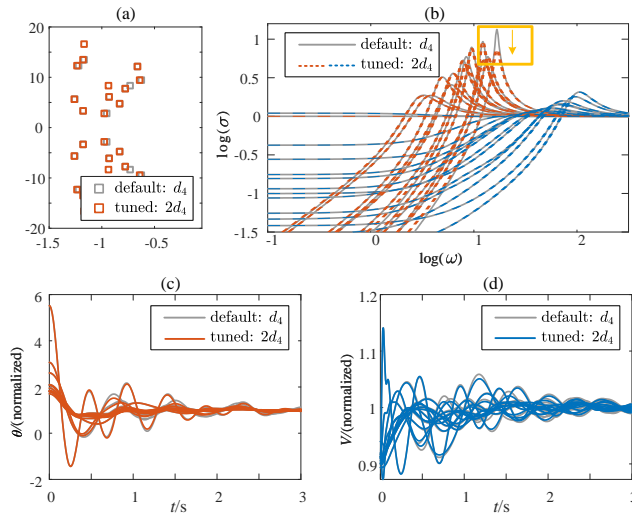


Fig. 12. Phase-angle control parameter tuning based on the proposed mechanism. The frequency damping  $d$  of the 4th device is doubled after the tuning. (a): state-space eigenvalue distribution before and after tuning. In all subplots, the gray lines represent the default system generated in Fig.6, while the colored lines represent the tuned system. (b): distribution of sensitivity  $S(s)$ , where the orange and blue lines respectively represent the phase-angle-related and voltage-related sensitivity. The yellow square shows the changes in the original maximum sensitivity after tuning. (c) and (d): the time-domain simulation results of phase-angle and voltage dynamics, respectively. All quantities are normalized with their steady-state values after disturbance to show the transient dynamics.

†: The system and disturbance setting methods are the same as Fig.7 with disturbance direction  $\varphi = 45^\circ$ .

stability of the whole system. The time-domain simulations are provided in Fig.13(c) and (d). After voltage dynamics tuning, while the phase-angle oscillation amplitudes are smaller, the voltage dynamics rarely change. Therefore, the stability of the whole system is improved with the parameter tuning based on the proposed theory.

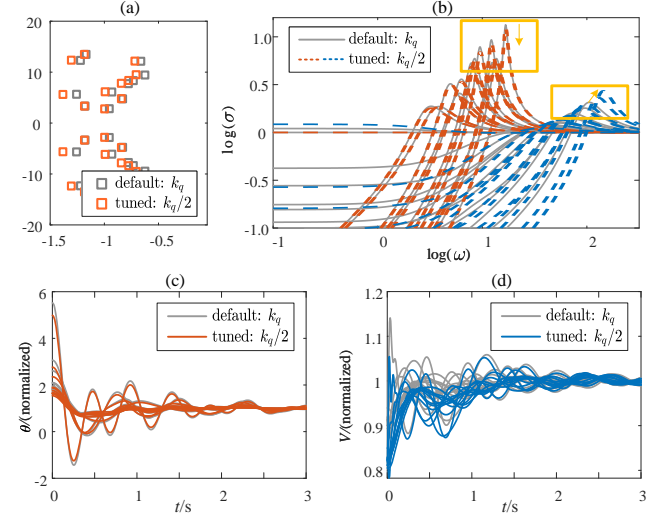


Fig. 13. Voltage control parameter tuning based on the proposed mechanism. The voltage droop strengths  $k_q$  of all devices are scaled with  $k'_q = k_q/2$  after the tuning. (a): state-space eigenvalue distribution before and after tuning. In all subplots, the gray lines represent the default system generated in Fig.6, while the colored lines represent the tuned system. (b): distribution of sensitivity  $S(s)$ , where the orange and blue lines respectively represent the phase-angle-related and voltage-related sensitivity. (c) and (d): the time-domain simulation results of phase-angle and voltage dynamics, respectively. All quantities are normalized with their steady-state values after disturbance to show the transient dynamics.